Theory of optical spin orientation in silicon

J. L. Cheng,[1,2] J. Rioux,[1] J. Fabian,[3] and J. E. Sipe[1,*]

[1]*Department of Physics and Institute for Optical Sciences, University of Toronto, 60 St. George Street, Toronto, Ontario, Canada M5S 1A7*
[2]*Hefei National Laboratory for Physical Sciences at Microscale, University of Science and Technology of China, Hefei, Anhui 230026, China*
[3]*Institute for Theoretical Physics, University of Regensburg, 93040 Regensburg, Germany*
(Received 11 March 2011; published 29 April 2011)

We theoretically investigate the indirect optical injection of carriers and spins in bulk silicon, using an empirical pseudopotential description of electron states and an adiabatic bond charge model for phonon states. We identify the selection rules, the contribution to the carrier and spin injection in each conduction band valley from each phonon branch and each valence band, and the temperature dependence of these processes. The transition from the heavy hole band to the lowest conduction band dominates the injection due to the large joint density of states. For incident light propagating along the [00$\bar{1}$] direction, the injection rates and the degree of spin polarization of injected electrons show strong valley anisotropy. The maximum degree of spin polarization is at the injection edge with values 25% at low temperature and 15% at high temperature.

I. INTRODUCTION

The optical injection of carriers is a powerful method for the study of the properties of semiconductors, and the optical injection of spins, i.e., optical orientation,[1] is an important element in the toolkit of the field of spintronics.[2–4] Most research has been focused on direct optical transitions. There have been fewer studies of indirect optical transitions, in which the excited electron and hole have different wave vectors, and phonon emission or absorption processes are necessary to conserve the total wave vector. In this paper, we consider the indirect optical injection of carriers and spins in bulk silicon.

Macfarlane *et al.*[5] first measured the fine structure of the absorption-edge spectrum in intrinsic bulk germanium and silicon in 1958 and identified the phonon-assisted indirect gap absorption branches. Thereafter, these studies were extended to doped silicon.[6–10] Theoretically, Elliott[11] was the first to study indirect absorption of excitons under the effective mass approximation and identified the absorption line shapes at photon energy near and far away from the indirect gap. He found that the line shapes are not sensitive to exciton effects at high photon energy. The electroabsorption in indirect gap semiconductor[12,13] and the absorption spectra of multiexciton-impurity complexes[14] were also investigated. Hartman[15] determined the absorption spectra using a parabolic band approximation. Dunn[16] and Chow[17,18] used a Green function method to investigate the physical processes in indirect absorption. All these models approximated the matrix elements of the electron-phonon interaction by their band-edge values. Later, pseudopotential models[19–23] were employed to calculate the transition matrix elements of the electron-phonon interaction around the band edge. However, a full band-structure calculation of the full spectrum of indirect gap absorption is still absent, even with the neglect of the excitonic effects.

Investigations of indirect optical spin injection are less common than those of indirect gap carrier injection. They are also less common than those of direct gap spin injection,[24] despite the fact that the first optical orientation experiment,[25] performed by Lampel in his study of the nuclear polarization of [29]Si in bulk silicon, employed indirect absorption. The degree of spin polarization in such an injection process is sometimes understood as a spin-dependent virtual optical transition combined with a spin-independent phonon absorption or emission process.[26,27] However, due to spin-orbit coupling the electron states are not pure spin eigenstates, and the effect of the electron-phonon interaction on the indirect gap injection needs to be calculated in detail. While Li and Dery[28] have recently studied the degree of circular polarization of the luminescence associated with the recombination across the indirect band gap following the electrical injection of spins in silicon, a theoretical investigation of indirect optical spin injection is still absent.

In the present paper, we perform a full band-structure calculation of the indirect optical injection of carriers and spins using an empirical pseudopotential model[29–31] (EPM) for electron states and an adiabatic bond charge model[32] (ABCM) for phonon states. Compared to $k \cdot p$ models and *ab initio* models, which are widely used for direct gap carrier and spin-injection calculation,[24,33] the advantage of the EPM is that the electron-phonon interaction in the whole Brillouin zone can be calculated consistently in combination with the ABCM. This approach has been successfully used to describe spin-relaxation processes[34] and photoluminescence[28] in bulk silicon.

We focus on the calculated optical indirect injection coefficients of carriers and spins, identifying the contribution from each valence band and phonon branch. We take the excited electrons and holes as free carriers. Because the electron-hole interaction is nearly spin independent, to good approximation it should affect the spin-injection and the carrier-injection rates in the same way and not affect the degree of spin polarization (DSP) of the injected electrons, which is the ratio of these two quantities. The dependence of the injection coefficients and DSP on photon energy, conduction band valley, and temperature are established. For the injection of carriers, our numerical results agree with the experiments at high photon energy. In the course of our investigations we also discuss in detail a simple but widely used model, in which the values of the transition matrix elements are approximated by their values at the band edge, and we compare its predictions with our calculations.

We organize the paper as follow: We begin with the general formula for indirect carrier and spin injection assisted by phonon emission and absorption in bulk silicon in Sec. II. Then the selection rules that follow from the crystal symmetry are discussed in Sec. III. We introduce the EPM and ABCM models in Sec. IV. Finally, we present our results and conclusions in Secs. V and VI. In the Appendix, we describe an improved adaptive linear analytic tetrahedral integration method (LATM)[24,35] that we use to perform the sixfold integration over the Brillouin zone (BZ).

II. MODEL FOR CARRIER AND SPIN INJECTION BY INDIRECT ABSORPTION

Figure 1 shows the band structure of silicon in the energy range $[-12$ eV, 6 eV] calculated from the EPM; the details are given in Sec. IV. The lowest four bands are valence bands, of which the upper three are the heavy hole (HH), light hole (LH), and spin split-off (SO) bands. The valence band edge (red dot) is at the Γ point with $\bm{k}_v^0 = \bm{0}$. All other bands are conduction bands. From the figure, the conduction band edge (red filled square) is at $\bm{k}_c^0 \approx 0.85\overrightarrow{\Gamma X}$ on the Δ symmetry line and results in six equivalent valleys that can be denoted as $X, \bar{X}, Y, \bar{Y}, Z, \bar{Z}$, indicating the location of the valley center. The calculated direct band gap at the Γ point is $E_g = 3.4$ eV, while the indirect band gap is $E_{ig} = 1.17$ eV. When the photon energy satisfies $E_{ig} < \hbar\omega < E_g$, optical injection occurs only across the indirect gap. Because the excited electron and hole have different wave vectors, the transition must be assisted by phonon emission or absorption. The green and blue lines show two possible indirect gap transitions between the valence and conduction band edges. The red hollow square and circle indicate possible intermediate states.
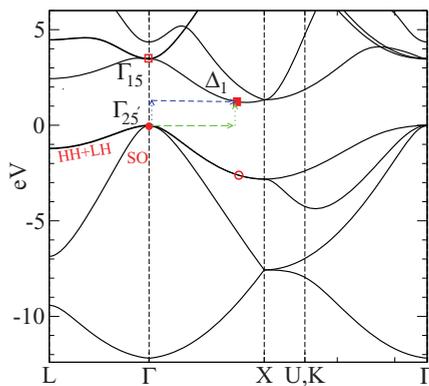

FIG. 1. (Color online) Band structure of silicon, calculated from the EPM, with symmetry notation at the Γ point and the conduction band edge (Δ_1). The valence band is noted by HH, LH, and SO bands. Two important phonon-assisted transitions from valence band edge (red dot) to conduction band edge (red filled square) are given by green lines and blue lines. The dotted lines refer to optical transitions, while the dashed lines refer to the transitions mediated by phonons. The red hollow square (circle) stands for one of the possible intermediated states in the transition given by blue (green) lines.

For an electric field $\bm{E}(t) = \bm{E}_\omega e^{-i\omega t} + \text{c.c.}$, the carrier- and spin-injection rates in silicon can be generally written as

$$\dot{n}(T,\omega) = \xi^{ab}(T,\omega)E_\omega^a \left(E_\omega^b\right)^*,$$
$$\dot{S}^f(T,\omega) = \zeta^{fab}(T,\omega)E_\omega^a \left(E_\omega^b\right)^*. \tag{1}$$

Here $\xi^{ab}(T,\omega)$ and $\zeta^{fab}(T,\omega)$ are the injection coefficients for carriers and spins, respectively, at temperature T. The superscript Roman characters indicate Cartesian coordinates, and repeated superscripts are to be summed over.

Using Fermi's golden rule, we find the injection coefficient ξ^{ab} and ζ^{fab} to be of the form

$$\mathcal{A}^{ab} = \sum_{I;cv\lambda\pm} \mathcal{A}_{I;cv\lambda\pm}^{ab}, \tag{2}$$

with

$$\mathcal{A}_{I;cv\lambda\pm}^{ab} = \frac{2\pi}{\hbar} \sum_{\bm{k}_c \in I, \bm{k}_v} \delta(\varepsilon_{c\bm{k}_c} - \varepsilon_{v\bm{k}_v} \pm \hbar\Omega_{(\bm{k}_c - \bm{k}_v)\lambda} - \hbar\omega)$$
$$\times N_{(\bm{k}_c - \bm{k}_v)\lambda\pm} \mathcal{A}_{c\bm{k}_c v\bm{k}_v;\lambda}^{ab}, \tag{3}$$

where

$$\mathcal{A}_{c\bm{k}_c v\bm{k}_v;\lambda}^{ab} = \sum_{\sigma_c\sigma_c'\sigma_v} \langle \bar{c}'\bm{k}_c|\hat{\mathcal{A}}|\bar{c}\bm{k}_c\rangle T_{\bar{c}\bm{k}_c\bar{v}\bm{k}_v\lambda}^a \left(T_{\bar{c}'\bm{k}_c\bar{v}\bm{k}_v\lambda}^b\right)^*. \tag{4}$$

Here I is the valley index; $c(v)$ is the conduction (valence) band index without including spin; $\bm{k}_c$ ($\bm{k}_v$) is the electron (hole) wave vector, where $\bm{k}_c \in I$ means the summation is over the Ith valley; $\varepsilon_{c\bm{k}_c}(\varepsilon_{v\bm{k}_v})$ give the energy spectra of conduction (valence) bands; $\hbar\Omega_{\bm{q}\lambda}$ gives the phonon energy at wave vector $\bm{q}$ and mode λ [longitudinal optical (LO) and acoustic (LA), and transverse optical (TO) and acoustic (TA) branches]; and $N_{\bm{q}\lambda\pm} = N_{\bm{q}\lambda} + \frac{1}{2} \pm \frac{1}{2}$, where $N_{\bm{q}\lambda}$ is the equilibrium phonon number. The operator $\hat{\mathcal{A}}$ in Eq. (4) stands for the identity operator $\hat{I}$ in the carrier injection calculation, and the fth component of the spin operator in the spin-injection calculation. The indirect optical transition matrix elements are

$$T_{\bar{c}\bm{k}_c\bar{v}\bm{k}_v\lambda}^a = \frac{e}{\hbar\omega}\sum_{\bar{n}} \left\{ \frac{M_{\bar{c}\bm{k}_c\bar{n}\bm{k}_v,\lambda}v_{\bar{n}\bar{v}\bm{k}_v}^a}{\omega - \omega_{nv\bm{k}_v}} + \frac{v_{\bar{c}\bar{n}\bm{k}_c}^a M_{\bar{n}\bm{k}_c\bar{v}\bm{k}_v,\lambda}}{\omega_{cn\bm{k}_c} - \omega} \right\}, \tag{5}$$

in which $\bar{c} = \{c,\sigma_c\}$, $\bar{c}' = \{c,\sigma_c'\}$, $\bar{v} = \{v,\sigma_v\}$, and $\bar{n} = \{n,\sigma_n\}$ are full band indexes, with $\sigma_c,\sigma_c',\sigma_v$ being the spin indexes; $\varepsilon_{n\bm{k}}$ is the electron energy at band n and wave vector $\bm{k}$, and $\omega_{nm\bm{k}}$ is defined by $\hbar\omega_{nm\bm{k}} \equiv \varepsilon_{n\bm{k}} - \varepsilon_{m\bm{k}}$. The velocity matrix elements are given by $\bm{v}_{\bar{n}\bar{m}\bm{k}} = \langle \bar{n}\bm{k}|\hat{\bm{v}}|\bar{m}\bm{k}\rangle$, with the velocity operator $\hat{\bm{v}} = \partial H_e/\partial\bm{p}$ and the unperturbed electron Hamiltonian H_e; $M_{\bar{n}\bm{k}_c\bar{m}\bm{k}_v,\lambda} = \langle \bar{n}\bm{k}_c|H_\lambda^{\text{ep}}(\bm{k}_c - \bm{k}_v)|\bar{m}\bm{k}_v\rangle$ are matrix elements of the electron-phonon interaction H^{ep}, which is written as $H^{\text{ep}} = \sum_{\bm{q}\lambda} H_\lambda^{\text{ep}}(\bm{q})(a_{\bm{q}\lambda} + a_{-\bm{q}\lambda}^\dagger)$, with $a_{\bm{q}\lambda}$ being the phonon annihilation operator for wave vector $\bm{q}$ and mode λ.

We now turn to the symmetry properties of $\mathcal{A}_{I;cv\lambda\pm}^{ab}$. Though bulk silicon has O_h symmetry, each conduction-band valley only has C_{4v} symmetry.[36] Therefore each $\mathcal{A}_{I;cv\lambda\pm}$ only has C_{4v} symmetry, since the summation over $\bm{k}_c$ is limited to $\bm{k}_c$ in the Ith valley. The summation of Eq. (3) can be rewritten as

$$\mathcal{A}_{I;cv\lambda\pm}^{ab} = \frac{2\pi}{\hbar}\mathcal{N}_v\mathcal{N}_{c,I}\sum_{\bm{k}_c \in I}{}' \sum_{\bm{k}_v}{}' \frac{1}{\mathcal{N}_v}\sum_{P_v}\delta(\varepsilon_{c\bm{k}_c} - \varepsilon_{v\bm{k}_v}$$
$$\pm \hbar\Omega_{(\bm{k}_c - P_v\bm{k}_v)\lambda} - \hbar\omega)N_{(\bm{k}_c - P_v\bm{k}_v)\lambda\pm}$$
$$\times \tilde{\mathcal{A}}_{I;c\bm{k}_c v(P_v\bm{k}_v)\lambda}^{ab}, \tag{6}$$

where

$$\tilde{\mathcal{A}}_{I;ck_cvk_v\lambda}^{ab} = \frac{1}{\mathcal{N}_{c,I}} {\sum_{P_{c,I}}}' \mathcal{A}_{c(P_{c,I}k_c)v(P_{c,I}k_v);\lambda}^{ab}. \qquad (7)$$

The prime indicates the summation is only over the irreducible wedge of the Brillouin zone, $P_{c,I}$ are the $\mathcal{N}_{c,I}$ symmetry operations in C_{4v} that keep the Ith valley unchanged, while P_v are the $\mathcal{N}_v$ symmetry operations in O_h. For each process $\{I;cv\lambda\pm\}$, the symmetry properties of the tensor with components $\mathcal{A}_{I;cv\lambda\pm}^{ab}$ are the same as those of the tensor with components $\tilde{\mathcal{A}}_{I;ck_cvk_v\lambda}^{ab}$. Therefore, in the $I = Z$ valley, the $\xi_{Z;cv\lambda\pm}^{ab}$ form a second rank tensor with only two nonzero independent components,

$$\begin{aligned} \xi_{Z;cv\lambda\pm}^{xx} &= \xi_{Z;cv\lambda\pm}^{yy} \equiv \xi_{cv\lambda\pm}^{(1)}, \\ \xi_{Z;cv\lambda\pm}^{zz} &\equiv \xi_{cv\lambda\pm}^{(2)}. \end{aligned} \qquad (8)$$

Similarly, the $\zeta_{Z;cv\lambda}^{abc}$ form a third-rank pseudotensor with only two nonzero independent components,

$$\begin{aligned} \zeta_{Z;cv\lambda\pm}^{zxy} &= -\zeta_{Z;cv\lambda\pm}^{zyx} \equiv i\zeta_{cv\lambda\pm}^{(1)}, \\ \zeta_{Z;cv\lambda\pm}^{xyz} &= -\zeta_{Z;cv\lambda\pm}^{yxz} \equiv i\zeta_{cv\lambda\pm}^{(2)}, \\ \zeta_{Z;cv\lambda\pm}^{xzy} &= -\zeta_{Z;cv\lambda\pm}^{yzx} = -i\zeta_{cv\lambda\pm}^{(2)}, \end{aligned} \qquad (9)$$

where $\xi^{(1)}$, $\xi^{(2)}$, and $\zeta^{(1)}$ are real numbers and $\zeta^{(2)}$ is also a real number because of inversion and time-reversal symmetry in bulk silicon. The injection coefficients in other valleys can be obtained by properly rotating the Z valley to the corresponding valley. The total injection coefficients

$$\mathcal{A}_{cv\lambda\pm}^{ab} = \sum_I \mathcal{A}_{I;cv\lambda\pm}^{ab} \qquad (10)$$

have higher symmetry, and the nonzero components satisfy

$$\begin{aligned} \xi_{cv\lambda\pm}^{xx} &= \xi_{cv\lambda\pm}^{yy} = \xi_{cv\lambda\pm}^{zz} = 2\xi_{cv\lambda\pm}^{(2)} + 4\xi_{cv\lambda\pm}^{(1)}, \\ \zeta_{cv\lambda\pm}^{xyz} &= \zeta_{cv\lambda\pm}^{yzx} = \zeta_{cv\lambda\pm}^{zxy} = -\zeta_{cv\lambda\pm}^{xzy} = -\zeta_{cv\lambda\pm}^{zyx} = -\zeta_{cv\lambda\pm}^{yxz} \\ &= i\big(2\zeta_{cv\lambda\pm}^{(1)} + 4\zeta_{cv\lambda\pm}^{(2)}\big). \end{aligned}$$

All quantities keep the identified symmetry properties on summation of one or several subscripts in $\{cv\lambda\pm\}$.

III. TRANSITIONS AT THE BAND EDGE

The values of the matrix elements $\boldsymbol{T}_{\bar{c}k_c\bar{v}k_v,\lambda}$ at the band edge, $\boldsymbol{T}_{\bar{c}k_c^0\bar{v}k_v^0,\lambda}$, provide insight into the importance of each injection process. For the indirect gap injection in silicon, the conduction band edge in the Z valley is at $\boldsymbol{k}_c^0 = (0,0,k_\Delta)$, while the valence band edge is at the Γ point, $\boldsymbol{k}_v^0 = 0$. In analyzing transitions near the band edge, we can use the following two approximations: (i) the values of the transition matrix elements [Eq. (4)] are taken at their band-edge values and (ii) the values of the wave vector, the energy, and the phonon number of the phonons involved are all taken at their band-edge values. Under these approximations, Eq. (6) becomes

$$\mathcal{A}_{I;cv\tau\pm}^{ab}(T,\omega) \approx \frac{2\pi}{\hbar} J_{cv}\big(\hbar\omega \mp \hbar\Omega_{\boldsymbol{k}_c^0\lambda}\big) N_{\boldsymbol{k}_c^0\tau\pm} \bar{\mathcal{A}}_{I;cv\tau}^{ab}, \qquad (11)$$

with

$$J_{cv}(\hbar\omega) = \sum_{\boldsymbol{k}_c \in I, \boldsymbol{k}_v} \delta(\varepsilon_{c\boldsymbol{k}_c} - \varepsilon_{v\boldsymbol{k}_v} - \hbar\omega), \qquad (12)$$

$$\bar{\mathcal{A}}_{I;cv\tau}^{ab} = \frac{1}{\mathcal{N}_v} \sum_{\lambda \in \tau} \sum_{P_v} \tilde{\mathcal{A}}_{ck_c^0 v(P_v k_v^0)\lambda}^{ab}. \qquad (13)$$

Here τ indicates the phonon branches (TA, TO, LA, LO), $J_{cv}(\hbar\omega)$ is the joint density of states (JDOS) for indirect gap injection, $\bar{\mathcal{A}}_{I;cv\tau}^{ab}$ gives the symmetrized transition matrix elements at the band edge, and $\sum_{\lambda \in \tau}$ indicates summation over all modes in the τth branch. Under the parabolic band approximation,[15] the JDOS is

$$J_{cv}(\hbar\omega) \propto (E_{\text{ig}} - \hbar\omega)^2. \qquad (14)$$

We now turn to $\bar{\mathcal{A}}_{I;cv\tau}^{ab}$. Because the HH and LH bands are degenerate at the Γ point and their wave functions are not uniquely determined, unambiguous values of $\mathcal{A}_{ck_c^0 vk_v^0\lambda}^{ab}$ and $\tilde{\mathcal{A}}_{ck_c^0 vk_v^0\lambda}^{ab}$ for the HH and LH bands separately do not exist at the band edge. But this is not a problem for $\bar{\mathcal{A}}_{I;cv\tau}^{ab}$, due to the summation over all symmetry operations. To show this clearly, we indicate all intermediate states in the transition matrix elements implicitly by writing

$$\boldsymbol{T}_{\bar{c}k_c\bar{v}k_v;\lambda} = \frac{e}{\omega} \langle \bar{c}k_c | \hat{\boldsymbol{T}}_{ck_cvk_v;\lambda} | \bar{v}k_v \rangle, \qquad (15)$$

with the operator

$$\begin{aligned} \hat{\boldsymbol{T}}_{ck_cvk_v;\lambda} &\equiv H_\lambda^{\text{ep}}(\boldsymbol{k}_c - \boldsymbol{k}_v) \frac{1}{\hbar\omega - H_e + \varepsilon_{vk_v}} \hat{\boldsymbol{v}} \\ &+ \hat{\boldsymbol{v}} \frac{1}{\varepsilon_{ck_c} - H_e - \hbar\omega} H_\lambda^{ep}(\boldsymbol{k}_c - \boldsymbol{k}_v). \quad (16) \end{aligned}$$

Substituting Eq. (15) into Eq. (4), it is easy to find that the expression for $\bar{\mathcal{A}}_{I;cv\tau}^{ab}$ includes a summation $\mathcal{N}_v^{-1} \sum_{P_v} P_v |\bar{v}k_v^0\rangle\langle\bar{v}k_v^0| P_v$, which equals $\sum_{\bar{v}' \in \text{LH,HH}} |\bar{v}'k_v^0\rangle \langle\bar{v}'k_v^0|/4$ when v is the HH or LH band. So $\bar{\mathcal{A}}_{I;c\text{HH}\tau}^{ab} = \bar{\mathcal{A}}_{I;c\text{LH}\tau}^{ab} = (\bar{\mathcal{A}}_{I;c\text{HH}\tau}^{ab} + \bar{\mathcal{A}}_{I;c\text{LH}\tau}^{ab})/2$ are unambiguous and give the same value for both the HH and LH bands. This conclusion mirrors a similar one in the study of injection across the direct gap.[24] In the following, we focus on selection rules for $\bar{\mathcal{A}}_{Z;cv\lambda}^{ab}$. Li and Dery[28] also discussed the selection rules in the context of luminescence by considering only the lowest conduction band and the highest valence band as the intermediate states; they also assume equal amplitudes for the two interference processes shown in Fig. 1. Here we give a general discussion using Eq. (15), without relying on the properties of the intermediate states.

Without spin-orbit coupling, the valence band states at the Γ point transform according to the representation Γ_{25}' (with basis functions that transform as $\{yz,zx,xy\}$, which are labeled as $\{\mathcal{X},\mathcal{Y},\mathcal{Z}\}$ here).[24] We first consider the electron states that lie in the Z valley, in which the conduction band-edge state transforms according to the representation Δ_1 (basis function $\{z\}$).[36] The phonon states involved transform according to the representation Δ_1 (basis function $\{z\}$) for the LA phonon mode, Δ_2' (basis function $\{x^2 - y^2\}$) for the LO phonon mode and Δ_5 (basis functions $\{x,y\}$) for the TA/TO phonon modes;[36] $H_\lambda^{ep}(\boldsymbol{k}_c^0)$ has the same symmetry properties as the λth branch phonon polarization vector. The velocity $\hat{\boldsymbol{v}}$ transforms according to the representation $\Delta_1 \oplus \Delta_2$. All nonzero components of the vector $\boldsymbol{T}_{ck_c^0vk_v^0\lambda}$ are listed in Table I for the different valence bands and phonon modes. There are

TABLE I. The transition matrix elements ($T^x_{ck^0_c,vk^0_v,\lambda}$, $T^y_{ck^0_c,vk^0_v,\lambda}$, $T^z_{ck^0_c,vk^0_v,\lambda}$). All quantities can be taken as real numbers. We use ($T^{(')}_1$, $T^{(')}_2$) to refer to (T_1, T_2) (TA phonon) or (T'_1, T'_2) (TO phonon) as appropriate.

| $\boldsymbol{T}_{ck^0_c vk^0_v\lambda}$ | Phonon mode λ | | | |
| | TA/TO | | LA | LO |
	x	y	z	$x^2 - y^2$
$\lvert\mathcal{X}\rangle$	0	$(0,0,T^{(')}_1)$	$(0,T_3,0)$	$(T_4,0,0)$
$\lvert\mathcal{Y}\rangle$	$(0,0,T^{(')}_1)$	0	$(T_3,0,0)$	$(0,T_4,0)$
$\lvert\mathcal{Z}\rangle$	$(0,T^{(')}_2,0)$	$(T^{(')}_2,0,0)$	0	$(0,0,T_5)$

totally seven nonzero quantities: T_1 and T_2 for TA phonon, T'_1 and T'_2 for TO phonon, T_3 for LA phonon, and T_4 and T_5 for LO phonon. In Li and Dery's approximations, $T_2 = 2T_1$ and $T'_2 = 2T'_1$ because the two transition processes summed are of equal magnitude, and T_5 vanishes due to their limitation of the intermediate states. In contrast, we keep all nonzero terms in our treatment and give their values in Sec. IV.

With spin-orbit coupling, the valence bands at the Γ point are split into HH ($\lvert\frac{3}{2}, \pm\frac{3}{2}\rangle$), LH ($\lvert\frac{3}{2}, \pm\frac{1}{2}\rangle$), and SO ($\lvert\frac{1}{2}, \pm\frac{1}{2}\rangle$) bands with the following states:

$$\left\lvert\frac{1}{2}, +\frac{1}{2}\right\rangle = \frac{1}{\sqrt{3}}\left\lvert\mathcal{Z}\rangle\vert\uparrow\rangle + \frac{1}{\sqrt{3}}\vert\mathcal{X}+i\mathcal{Y}\rangle\vert\downarrow\rangle,$$

$$\left\lvert\frac{1}{2}, -\frac{1}{2}\right\rangle = \frac{1}{\sqrt{3}}\vert\mathcal{X}-i\mathcal{Y}\rangle\vert\uparrow\rangle - \frac{1}{\sqrt{3}}\vert\mathcal{Z}\rangle\vert\downarrow\rangle,$$

$$\left\lvert\frac{3}{2}, +\frac{1}{2}\right\rangle = \sqrt{\frac{2}{3}}\vert\mathcal{Z}\rangle\vert\uparrow\rangle - \frac{1}{\sqrt{6}}\vert\mathcal{X}+i\mathcal{Y}\rangle\vert\downarrow\rangle,$$

$$\left\lvert\frac{3}{2}, -\frac{1}{2}\right\rangle = \frac{1}{\sqrt{6}}\vert\mathcal{X}-i\mathcal{Y}\rangle\vert\uparrow\rangle + \sqrt{\frac{2}{3}}\vert\mathcal{Z}\rangle\vert\downarrow\rangle, \qquad (17)$$

$$\left\lvert\frac{3}{2}, +\frac{3}{2}\right\rangle = -\frac{1}{\sqrt{2}}\vert\mathcal{X}+i\mathcal{Y}\rangle\vert\uparrow\rangle,$$

$$\left\lvert\frac{3}{2}, -\frac{3}{2}\right\rangle = \frac{1}{\sqrt{2}}\vert\mathcal{X}-i\mathcal{Y}\rangle\vert\downarrow\rangle.$$

The SO band at the Γ point is lower than the degenerate HH and LH bands by 44 meV. At the conduction band edge, the states can be approximately written as $\vert z\uparrow\rangle$ and $\vert z\downarrow\rangle$ due to the very small spin mixing. The transition matrix elements between these states with spin-orbit coupling can be obtained by linearly combining the terms in Table I.

For σ^- light, $\boldsymbol{E} = (\hat{\boldsymbol{x}} - i\hat{\boldsymbol{y}})/\sqrt{2}$, we show in Fig. 2 the possible optical transitions from the valence bands to the Z valley of the conduction band. Here the spin quantization directions of both electrons and holes are chosen along the z direction. It is obvious that the phonon states play a key role in these transitions. For transitions from HH and LH bands, the LA and LO phonon-assisted processes inject spin polarization along the $-z$ and z directions, respectively, with a DSP of 50%, yet there is no spin polarization from the TA/TO phonon-assisted processes. Despite its spin independence, the electron-phonon interaction still affects the selection rules for spin injection since all states involved are not pure spin states due to spin-orbit coupling. Therefore, it is not adequate to treat the indirect transitions as a spin-dependent virtual optical
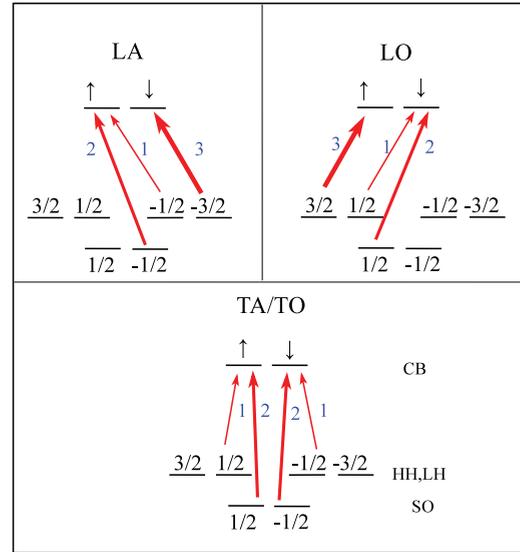

FIG. 2. (Color online) Diagram for optical indirect transitions from the band edge of the valence bands (HH, LO, and SO) to the band edge of the conduction band (CB) in the Z valley, under σ^- light. Both the hole and electron states are quantized along the z direction. The red arrows stand for allowed transitions, whose probabilities are proportional to the product of the numbers next to the arrows and factors of $\frac{1}{3}T_3^2$, $\frac{1}{3}T_4^2$, $\frac{1}{3}[T_2]^2$, and $\frac{1}{3}[T'_2]^2$ for LA, LO, TA, and TO phonon-assisted processes, respectively.

transition combined with a phonon emission or absorption process that does not affect the spin.[26,27]

Now we look at the transitions to the electron states in the X valley. The possible optical transitions are complicated and are shown in Fig. 3. To simplify the diagram, we choose the quantization axis of the hole states along the x direction and that of the electron states along the z direction. Here the LO and TA/TO phonons can play a role in spin injection, but the LA phonon cannot. Thus there is strong valley anisotropy in the injection of spins. In Li and Dery's approximations, the TA/TO phonon-assisted processes give a DSP of 1/3 from the HH and LH bands, and the LO phonon-assisted process gives no spin polarization. In our more detailed analysis, we cannot simply identify a DSP for each process, as some of these processes are determined by more than one nonzero parameter. We discuss the actual values of these at the end of Sec. IV.

Because the band-edge transitions strongly depend on the choice of the electron and hole states, it is constructive to give the nonzero components of $\bar{\mathcal{A}}^{ab}_{Z;cv\tau}$. They can be specified by giving the values of $\bar{\mathcal{A}}^{(1,2)}_{cv\tau}$, in terms of which $\bar{\mathcal{A}}^{ab}_{Z;cv\tau}$ are found following the pattern of Eqs. (8) and (9). The results are shown in Table II. In the calculation, we have used the result that the contributions for the HH and LH bands at the Γ point are exactly the same.

From Table II, we find that some results are similar to those for direct gap injection: The band-edge transition magnitudes for carrier injection are the same for each valence band, while the ones for spin injection are only identical for HH and LH bands and satisfy

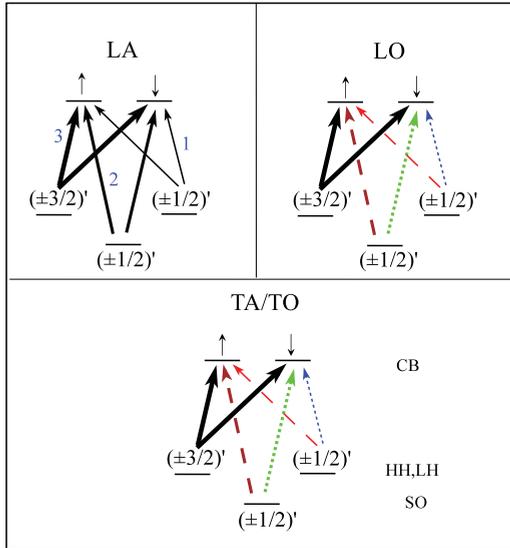$$\sum_v \bar{\xi}^{(1,2)}_{cv\tau} = 0. \qquad (18)$$

FIG. 3. (Color online) Diagram for optical indirect transitions from the band edge of the valence bands (HH, LO, and SO) to the band edge of the conduction band (CB) in the X valley, under σ^- light. The electron states are quantized along the z direction, and the prime beside the hole states indicate that they are quantized along the x direction. The transition strength for each color arrows in each phonon branch is as follows: In LA-assisted transitions, the factor is $\frac{1}{24}T_3^2$ for black arrows. In LO-assisted transitions, the factors are $\frac{1}{8}T_4^2$ for black arrows, $\frac{1}{24}(T_4 \pm 2T_5)^2$ for blue thin dotted $(+)$ and red thin dashed $(-)$ arrows, and $\frac{1}{12}(T_4 \pm T_5)^2$ for brown thick dashed $(+)$ and green thin dotted $(-)$ arrows. In TA-assisted transitions, the factors are $\frac{1}{4}[T_1]^2$ for black arrows, $\frac{1}{12}[T_1^2 + 2T_2^2 \pm 2T_2T_1]$ for red thin dashed $(+)$ and blue thin dotted $(-)$ arrows, and $\frac{1}{12}[2T_1^2 + T_2^2 \pm 2T_2T_1]$ for green thick dotted $(+)$ and brown thick dashed $(-)$ arrows. For TO-assisted processes the same formula hold with (T_1, T_2) replaced by (T_1', T_2').

The vanishing sum does not mean that the spin polarization becomes zero when the laser pulse is wide enough to involve all valence bands, because the densities of states for different valence bands differ. However, as the photon energy increases, the optical transition occurs away from the band edge, where the involved electron and hole states are superpositions of the band-edge states of all valence bands. As a consequence of Eq. (18), important band mixing leads to a small DSP.

TABLE II. Band-edge transition rates $(\bar{\mathcal{A}}_{cv\tau}^{(1)}, \bar{\mathcal{A}}_{cv\tau}^{(2)})$ with $\mathcal{A}$ being ξ for carrier injection and ζ for spin injection. We use $(T_1^{(')}, T_2^{(')})$ to refer to (T_1, T_2) (TA phonon) or (T_1', T_2') (TO phonon) as appropriate.

τ	TA/TO	LA	LO
		$\bar{\zeta}$	
SO	$(0, -\frac{2}{3}T_1^{(')}T_2^{(')})$	$(-\frac{2}{3}T_3^2, 0)$	$(\frac{2}{3}T_4^2, \frac{2}{3}T_4T_5)$
LH,HH	$(0, \frac{1}{3}T_1^{(')}T_2^{(')})$	$(\frac{1}{3}T_3^2, 0)$	$(-\frac{1}{3}T_4^2, -\frac{1}{3}T_4T_5)$
		$\bar{\xi}$	
SO	$(\frac{2}{3}[T_2^{(')}]^2, \frac{4}{3}[T_1^{(')}]^2)$	$(\frac{2}{3}T_3^2, 0)$	$(\frac{2}{3}T_4^2, \frac{2}{3}T_5^2)$
LH,HH	$(\frac{2}{3}[T_2^{(')}]^2, \frac{4}{3}[T_1^{(')}]^2)$	$(\frac{1}{3}T_3^2, 0)$	$(\frac{2}{3}T_4^2, \frac{2}{3}T_5^2)$

IV. MODEL FOR ELECTRON STATES AND PHONON STATES

To look at the carrier and spin injection away from the band edge, a full band structure model of the electron and phonon states is necessary. We use the EPM[29–31] for electron states and the ABCM[32] for phonon states. We describe these now and give the resulting electron-phonon interaction for indirect gap injection. In the EPM, electrons are described by the pseudo-Hamiltonian,

$$H_e = \frac{p^2}{2m_0} + \sum_{i\alpha} v(r - R_{i\alpha}). \quad (19)$$

Here p is the momentum operator; $R_{i\alpha} = R_i + \tau_\alpha$ is the equilibrium position for the αth ($\alpha = 1,2$) atom in the ith primitive cell located at R_i with $\tau_1 = 0$ and $\tau_2 = \frac{a}{4}(1,1,1)$, and a is the lattice constant; $v(r,p) = v_L(r) + v_{\text{NL}}(r,p) + v_{\text{so}}(r,p)$ is the atomic empirical pseudopotential, in which $v_L(r)$ and $v_{\text{NL}}(r,p)$ are the local and nonlocal spin-independent pseudopotentials, respectively,[29,30] and $v_{\text{so}}(r,p)$ is a spin-dependent contribution[31] introduced to fit the spin split-off energy at the Γ point.[34] Eigenstates of H_e are given by the Bloch states $|n\mathbf{k}\rangle = \sum_g c_{nk}(g)|\mathbf{k}+g\rangle$, where $|\mathbf{k}\rangle$ are plane wave states, g is a reciprocal lattice vector, and $c_{nk} = (c_{nk}^\uparrow \quad c_{nk}^\downarrow)^T$ are coefficients obtained by solving the single-particle Schrödinger equation.

The Fourier transform of the pseudopotential $v(r,p)$ is

$$v(k_1, k_2) = \int \frac{dr}{a^3} e^{-ik_1 \cdot r} v(r,p) e^{ik_2 \cdot r}. \quad (20)$$

For the local pseudopotential $v_L(r)$ taken to be of the form $v_L(r)$ with $r = |r|$, we have that $v_L(k_1, k_2)$ depends only on $|k_1 - k_2|$, and we write it as $v_L(|k_1 - k_2|)$. Chelikowsky and Cohen[29,30] showed that a suitable electron band structure can be produced by taking the values of $v_L(k)$ only at $k^2 = 3, 4$, and 11 $(2\pi/a)^2$, which lead to the conduction band energy at the X point of 1.17 eV. In order to produce the direct band gap E_g, the indirect band gap E_{ig}, and the location of the conduction band edge k_c^0 correctly after including the spin-orbit coupling, we use the following parameters $v_L(k) = -3.496, -0.544, 0.437, 0.429,$ and 0.1373 eV for $k^2 = 3, 4, 11, 16,$ and 19 $(2\pi/a)^2$. The calculated band structure is shown in Fig. 1. The calculation is for zero temperature. With increasing temperature, the electron-phonon interaction induces changes at the band edge and shifts the indirect and direct band gaps.[37–40] For silicon, the shift in the conduction band edge is minor; we absorb it into E_{ig} in the following.

For the phonons, the ABCM is used for calculating the polarization vectors $\epsilon_{q\lambda}^\alpha$ and energies $\hbar\Omega_{q\lambda}$. The calculated band structure fits the experiments well.[32] The energies of phonons with wave vector k_c^0, which are involved in the band-edge transition, are $\hbar\Omega_{k_c^0,\text{TA}} = 19$ meV, $\hbar\Omega_{k_c^0,\text{LA}} = 43$ meV, $\hbar\Omega_{k_c^0,\text{LO}} = 53$ meV, and $\hbar\Omega_{k_c^0,\text{TO}} = 57$ meV.

By shifting the atom position from the equilibrium position $R_{i\alpha}$ to $R_{i\alpha} + u_{i\alpha}$, and then expanding the electron Hamiltonian (19) to linear order in $u_{i\alpha}$, we identify the electron-phonon interaction as $H^{\text{ep}} = -\sum_{i\alpha} \nabla v(r - R_{i\alpha}) \cdot u_{i\alpha}$. The atomic

TABLE III. Relative band-edge values of all quantities listed in Table II for the phonon emission process. The photon energies for different phonon branches are taken as $\hbar\omega = E_{ig} + \hbar\Omega_{k_c^0\lambda}$. All values are normalized with respect to the value of $|T_2'|^2$ in case A. Its value is $(T_2')^2 = 1.8 \times 10^{-86}$ J^2 V^{-2} m^{-1}.

	TA			TO			LA	LO		
	T_1^2	T_2^2	$T_1 T_2$	$(T_1')^2$	$(T_2')^2$	$T_1' T_2'$	T_3^2	T_4^2	T_5^2	$T_4 T_5$
A	0.020	0.018	−0.019	0.131	1.000	−0.358	0.018	0.218	0.001	−0.014
B	0.066	0.090	−0.077	0.120	1.024	−0.348	0.020	0.192	0.026	−0.070

displacement is usually expanded by the phonon polarization vectors as

$$\boldsymbol{u}_{i\alpha} = \sum_{\boldsymbol{q}\in 1^{st}BZ,\lambda} \left(\frac{\hbar}{\rho\Omega_{\boldsymbol{q}\lambda}}\right)^{1/2} (a_{\boldsymbol{q}\lambda} + a_{-\boldsymbol{q}\lambda}^\dagger)\boldsymbol{\epsilon}_{\boldsymbol{q}\lambda}^\alpha e^{i\boldsymbol{q}\cdot\boldsymbol{R}_i}, \quad (21)$$

with ρ being the mass density of silicon. The transition matrix elements between different electron states are given as

$$M_{n_1\boldsymbol{k}_1 n_2\boldsymbol{k}_2,\lambda} = -i\sqrt{\frac{\hbar}{\rho\Omega_{\boldsymbol{q}\lambda}}} \sum_{\boldsymbol{g}_1\boldsymbol{g}_2} \left[\Delta\boldsymbol{k}\cdot\sum_\alpha \boldsymbol{\epsilon}_{\boldsymbol{q},\alpha}^\lambda e^{-i\Delta\boldsymbol{k}\cdot\boldsymbol{\tau}_\alpha}\right]$$
$$\times c_{n_2\boldsymbol{k}_2}^\dagger(\boldsymbol{g}_1)v(\boldsymbol{k}_1 + \boldsymbol{g}_1, \boldsymbol{k}_2 + \boldsymbol{g}_2)c_{n_2\boldsymbol{k}_2}(\boldsymbol{g}_2),$$
$$(22)$$

where $\boldsymbol{q} = \boldsymbol{k}_1 - \boldsymbol{k}_2$, $\Delta\boldsymbol{k} = \boldsymbol{k}_1 + \boldsymbol{g}_1 - \boldsymbol{k}_2 - \boldsymbol{g}_2$.

In calculating the matrix elements of the electron-phonon interaction given in Eq. (22), the values of $v_L(k)$ at all k points are necessary, and they are obtained using the natural cubic spline interpolation[41] on the discrete points given above and two further restrictions: the first is the value $v_L(0)$; the second is a cutoff at high k, $v_L(k > k_{cut}) = 0$, where k_{cut} is a cut-off value. Bednarek and Rössler[20] showed that the values assumed for $v_L(0)$ and k_{cut} strongly affect the calculated matrix elements of the electron-phonon interaction in Eq. (22). In our calculation, we find that the assumed value of k_{cut} does not significantly affect H^{ep} for $k_{cut} > 3k_F$, and we set $k_{cut} = 3k_F$. We show the dependence of indirect absorption on $v_L(0)$ in Tables III and IV by taking $v_L(0) = -\frac{2}{3}E_F$ (denoted as case A) and $v_L(0) = 0$ (case B). Here k_F and E_F are the Fermi wave vector and Fermi energy of the free electron gas appropriate to the valence electron density in silicon.

For carrier injection, the contributions from the phonon branches other than TA are essentially the same in case A and B, while for spin injection the phonon processes involving TA or LO phonons and electron injection into the X valley give contributions that depend strongly on the value of $v_L(0)$. The DSP for the LO phonon-assisted process is about 6% in case A and 32% in case B. Nevertheless, by far the most important contribution to indirect gap injection comes from the TO phonon-assisted process, which is almost independent of $v_L(0)$ for both carrier and spin injection. In the following, we use the parameters of case A.

Contrary to what was assumed in Li and Dery's results, our results show that $T_2 = 2T_1$ or $T_2' = 2T_1'$ cannot be well satisfied. But the calculated DSP for TA/TO phonon-assisted processes in the X valley is still close to 1/3. The value of T_5 is reasonably small.

V. CALCULATIONS

To obtain the injection rates, we can focus only on energies near the band edge and rely on Eq. (11) or numerically evaluate Eq. (6) using the results of a full band structure calculation. Both strategies require a six-dimensional integration over the electron and hole wave vectors ranging within the BZ. In the present work, we vary the photon energy $\hbar\omega$ to about 1.5 eV above E_{ig}, which results in an effective integration volume consisting of about 3/8 of the volume of the whole BZ, and a very demanding calculation. Similarly to the integration

TABLE IV. Band-edge values of $\bar{\mathcal{A}}_{cHH\lambda}^{(1,2)}$. The classification in Z and X valleys follows Eq. (23). All values are normalized with respect to the value of $|T_2'|^2$ in case A.

	Z valley			X valley			Total		
	$c^Z \equiv$ $\bar{\xi}_{cHH\lambda+}^{(1)}$	$s^Z \equiv$ $-\frac{2}{\hbar}\bar{\zeta}_{cHH\lambda+}^{(1)}$	$DSP^Z \equiv$ s^Z/c^Z	$c^X \equiv$ $\frac{1}{2}(\bar{\xi}_{cHH\lambda+}^{(1)} + \bar{\xi}_{cHH\lambda+}^{(1)})$	$s^X \equiv$ $-\frac{2}{\hbar}\bar{\zeta}_{cHH\lambda+}^{(2)}$	$DSP^X \equiv$ s^X/c^X	$c \equiv$ $4c^X + 2c^Z$	$s \equiv$ $4s^X + 2s^Z$	$DSP \equiv$ s/c
				A					
TA	0.0117	0	0	0.019	−0.006	−32%	0.100	−0.025	−25%
LA	0.0122	−0.0062	−51%	0.006	0.00022	4%	0.0488	−0.0115	−24%
LO	0.145	0.0727	50%	0.073	0.00473	6%	0.583	0.164	28%
TO	0.667	−0.0056	−1%	0.42	−0.119	−28%	3.01	−0.489	−16%
				B					
TA	0.0603	−0.00045	−1%	0.074	−0.026	−35%	0.42	−0.103	−25%
LA	0.0135	−0.0067	−50%	0.0068	0	0	0.054	−0.013	−24%
LO	0.128	0.064	50%	0.072	0.023	32%	0.546	0.222	41%
TO	0.682	0	0	0.421	−0.116	−28%	3.05	−0.475	−16%

used in the calculation of direct gap injection, the integrand here is composed of an energy conservation term, i.e., the Dirac δ function, and a transition matrix element term. In a calculation of direct gap injection, the δ function is evaluated using a LATM[24,35] on a very fine grid, and the transition matrix elements are calculated on each grid point. However, this method is not practical in a calculation of indirect gap injection, because the transition matrix elements are too complicated to be evaluated on each point of a fine grid. Instead, we find that we can obtain a converged result by using separate grids for these two terms, adopting a finer grid for the Dirac δ function and interpolating the transition matrix elements on a rougher grid. The details of this method are in the Appendix. In our calculation, the valence bands include HH, LH, and SO bands, the conduction bands include the lowest and the first excited conduction bands, and the intermediate states are chosen as the lowest 30 bands to ensure convergence.

The total carrier and spin injection from any pair of valence bands via an emission or absorption process involving a phonon of any branch, as well as the carrier and spin injection into any conduction band valley, are completely determined once the quantities $\xi_{cv\lambda\pm}^{(1,2)}$ and $\zeta_{cv\lambda\pm}^{(1,2)}$ are specified: The nonvanishing Cartesian tensor components follow from Eqs. (8) and (9), the sum over the different valleys follows from Eq. (10), and the full response tensors follow from Eq. (2); once these are determined the injection rates can be calculated from Eq. (1) for any light polarization. Instead of presenting our calculated results for $\xi_{cv\lambda\pm}^{(1,2)}$ and $\zeta_{cv\lambda\pm}^{(1,2)}$ below, we present instead

$$
\begin{aligned}
\xi_{cv\lambda\pm}^{(X)} &\equiv \tfrac{1}{2}\big[\xi_{cv\lambda\pm}^{(1)} + \xi_{cv\lambda\pm}^{(2)}\big], \\
\xi_{cv\lambda\pm}^{(Z)} &\equiv \xi_{cv\lambda\pm}^{(1)}, \\
\zeta_{cv\lambda\pm}^{(X)} &\equiv -\zeta_{cv\lambda\pm}^{(2)}, \\
\zeta_{cv\lambda\pm}^{(Z)} &\equiv -\zeta_{cv\lambda\pm}^{(1)}.
\end{aligned}
\tag{23}
$$

These are the terms that appear in a simple excitation scenario using σ^- light, as described in the following section. They correspond to the injection into different valleys via the different processes. Nonetheless, we stress that given the quantities in Eq. (23), we can construct the carrier and spin injection in Eq. (1) for any polarization using Eqs. (8), (9), and (2).

VI. RESULTS

In the following, we focus on injection under σ^- light. In this case, the six valleys can be divided into two sets: $\{Z, \bar{Z}\}$ and $\{X, \bar{X}, Y, \bar{Y}\}$. The injection is identical for all the valleys within each set. The carrier and spin injection from the valence band v into the conduction band c in the Ith valley via a λth-branch phonon emission $(+)$ or absorption $(-)$ are identified by $\dot{n}_{I;cv\lambda\pm}$ and $\dot{S}_{I;cv\lambda\pm}$, respectively, which are given from Eq. (23) as

$$
\begin{aligned}
\dot{n}_{I;cv\lambda\pm} &= \xi_{cv\lambda\pm}^{(I)}|E_0|^2, \\
\dot{S}_{I;cv\lambda\pm}^{z} &= \zeta_{cv\lambda\pm}^{(I)}|E_0|^2,
\end{aligned}
\tag{24}
$$

with $\dot{S}_{I;cv\lambda\pm}^{x/y} = 0$. Accordingly, the coefficients

$$
\xi = \sum_{I;cv\lambda\pm} \xi_{cv\lambda\pm}^{(I)}, \quad \xi^{(I)} = \sum_{cv\lambda\pm} \xi_{cv\lambda\pm}^{(I)},
$$

$$
\xi_{\tau}^{(I)} = \sum_{cv\pm;\lambda\in\tau} \xi_{I;cv\lambda\pm}^{(I)}, \quad \xi_{cv\tau}^{(I)} = \sum_{\pm;\lambda\in\tau} \xi_{cv\lambda\pm}^{(I)},
$$

are also used in the following to understand the injection properties. Here $\tau =$ TA, LA, LO, and TO are the phonon branches; as before, $\sum_{\lambda\in\tau}$ indicates to a sum over all phonon modes in the τth branch. Similar notation is used for the injection coefficients of spins. We find that the polarization direction of injected spins in each valley is parallel or antiparallel to the z direction. The DSP is defined as

$$
\text{DSP} = \frac{\zeta}{\hbar\xi/2}, \quad \text{DSP}_{\{\cdots\}}^{(I)} = \frac{\zeta_{\{\cdots\}}^{(I)}}{\hbar\xi_{\{\cdots\}}^{(I)}/2}.
\tag{25}
$$

Here $\{\cdots\}$ indicates the subscripts for $\text{DSP}^{(I)}$ are the same as that for $\xi^{(I)}$ and $\zeta^{(I)}$.

A. Carrier injection

1. Band-edge carrier injection at 4 K

We first study the carrier injection at the band edge at 4 K. For band-edge injection, only the transitions between the lowest conduction band and the valence bands need to be considered; the first excited conduction band is ignored due to its small density of states. At this low temperature, only the phonon emission process is important. In Fig. 4 we show the spectra of the total injection rate (black thick solid curve) as well as the injection rates in Z and X valleys (black thick dashed and dot-dashed curves). All injection rates increase with increasing photon energy. These results are consistent with the analytical results in Sec. III, where the injection rates around the band edge are approximately proportional to the JDOS. The difference between the injection rates in the Z and X valleys shows that the injection is valley anisotropic. To understand the contribution from each phonon branch, we plot phonon-resolved injection rates in Fig. 5. We find that each phonon-resolved spectrum has a shape similar to the total. In our calculation, the importance of the phonon-assisted
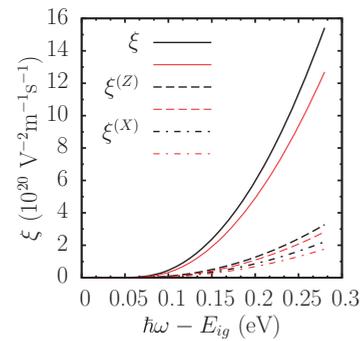

FIG. 4. (Color online) Spectra of carrier injection rates ξ (solid curves), $\xi^{(Z)}$ (dashed curves), and $\xi^{(X)}$ (dot-dashed curves) at 4 K. The black thick and red thin curves are the results calculated from Eq. (6) and Eq. (11), respectively.
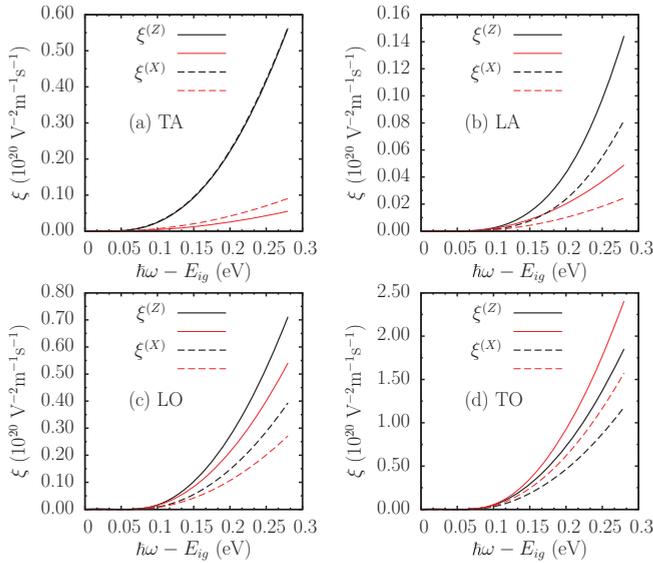
FIG. 5. (Color online) Phonon-resolved injection rates $\xi_\tau^{(Z)}$ (solid curves) and $\xi_\tau^{(X)}$ (dashed curves). The black thick and red thin curves are the results calculated from Eqs. (6) and (11), respectively.

processes are in order of TO > LO > TA > LA, in which the contribution of the LA-assisted process is less than 5%.

At the band edge, the injection rates can also be obtained from the simplified calculation given by Eq. (11), which can be used to identify how well the selection rules in Table II work. The results of the simplified calculation are also plotted in Figs. 4 and 5 as red thin curves. Compared to the full calculation, Fig. 5 shows that these results have smaller values for the TA, LA, and LO branches, and a larger value for the TO branch. The differences are significant for acoustic phonons and minor for optical phonons. Even for optical phonons, the difference is about 30% at excess photon energy of 0.25 eV. However, because the errors for the two most important phonon branches, i.e., TO and LO branches, are opposite, the difference in the total injection rates between these two methods is not so great. This difference illustrates not only the variation of the transition matrix elements on $\boldsymbol{k}_c$ and $\boldsymbol{k}_v$ but also the failure of the simplified formula at high photon energy. Nevertheless, the simplified formula gives the correct qualitative results.

To better understand the details of carrier injection, we also plot the contribution from each valence band to $\xi^{(X,Z)}$ for the TO-assisted process in Fig. 6. There are two important features: First, all injection rates increase with photon energy, which can be understood by the increase of the involved JDOS with photon energy. Second, the HH band gives the greatest contribution to the injection rate, and the SO band gives the smallest. As the transition matrix elements are the same for these three bands at the band edge, the magnitude is determined only by the density of states of each valence band. Similar results are obtained for the other three phonon branches.

2. Comparison with experiment at 4 K

Figure 7 gives the photon energy dependence of $\sqrt{\alpha(\omega)\hbar\omega}$ at $T = 4$ K. Here $\alpha(\omega) = \hbar\omega\xi(\omega)/(2n(\omega)c\epsilon_0)$ is the absorption coefficient, $n(\omega)$ is the refractive index of silicon, c is the
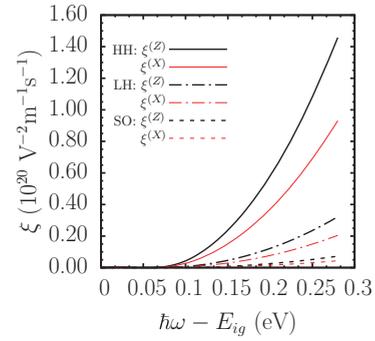

FIG. 6. (Color online) The contribution from each valence band to the injection rates $\xi^{(Z)}$ (thick curves) and $\xi^{(X)}$ (thin colored curves) for the TO-assisted process.

speed of light, and ϵ_0 is the vacuum permittivity. Our result (the solid curve) shows two important features of the indirect gap injection: Near the onset of absorption, for $\hbar\omega < E_{ig} + \hbar\Omega^0_{\boldsymbol{k}_c^0,\text{LO}}$, the TA phonon emission process dominates, and then the optical phonons make important contributions for $\hbar\omega > E_{ig} + \hbar\omega_{\boldsymbol{k}_c^0,\text{LO}}$. The separation between these two regions is indicated by the kink in the figure. In each region, the line shape of $\sqrt{\alpha\hbar\omega}$ is approximately a linear function of $\hbar\omega$, which is consistent with the results in the parabolic band approximation, i.e., $\sqrt{\alpha\hbar\omega} \propto \hbar\omega - E_{ig} - \hbar\Omega_{\boldsymbol{k}_c^0\lambda}$.[11,15] With respect to these features, our results match the experimental results very well.

Yet compared to the experiment by Macfarlane *et al.*,[5] our result fails to show the correct energy shift and line shape at the beginning of each region. Both of these features are related to the excitonic effect, which is absent in our calculation. When the excitonic effect is considered, both the bound and continuum exciton states contribute to the absorption, as discussed in detail by Elliott[11]: The onset of absorption is shifted to lower energy by the presence of exciton bound states and modified to give a line shape $\alpha \propto \sqrt{\hbar\omega - (E_{ig} + \hbar\Omega_{\boldsymbol{k}_c^0\lambda} - E_{ex})}$ associated with the first exciton bound state and each phonon branch, with an exciton bind energy $E_{ex} \approx -14$ meV[39]; the line shape of the absorption associated with the exciton continuum states is similar to that calculated without including the electron-hole interaction. Despite all this, in the next we will see that the absorption at high photon energy can still be well described by our model. Even at low photon energy, we expect our model can give
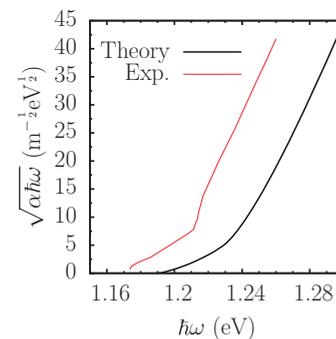

FIG. 7. (Color online) Spectra of $\sqrt{\alpha\hbar\omega}$. The solid curve is our theoretical result. The red thin curve is experimental data.[5]
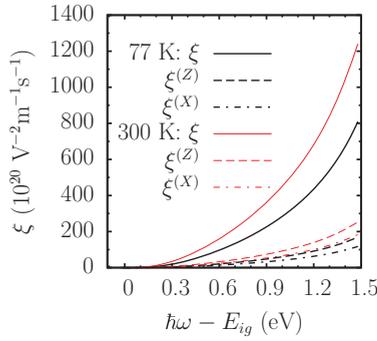
FIG. 8. (Color online) Spectra of ξ, $\xi^{(Z)}$, and $\xi^{(X)}$ at 77 K (black thick curves) and 300 K (red thin curves).

a reasonable description of the DSP, because the excitonic effects are, to good approximation, spin independent.

3. Carrier injection at high temperature

The indirect gap injection rates depend on the phonon number and thus on the temperature. With increasing temperature, the phonon absorption processes come into play, and the onset of the injection spectrum moves to lower photon energy. The equilibrium phonon numbers $N_{k_c^0 \lambda}$ at different temperatures are as follows: At 77 K, all phonon numbers can approximately be ignored, so only the emission processes occur. At 300 K, the phonon numbers become 0.92 for TA, 0.23 for LA, 0.15 for LO, and 0.12 for TO. Because the TA phonon has smaller energy, the absorption induced by the TA phonon-assisted process is the most temperature sensitive.

In Fig. 8 the spectra of ξ, $\xi^{(Z)}$, and $\xi^{(X)}$ are plotted for 77 K (black thick curves) and 300 K (red thin curves). All injection rates increase remarkably with temperature: ξ displays an approximately 50% increase when the excess photon energy is 1.5 eV. Note that the injection rates at 77 K and 4 K are approximately the same. The phonon-resolved absorption spectra at different temperatures are plotted in Fig. 9. The injection rate from each phonon branch increases with temperature, and the increment is most significant for the TA phonon branch. At 300 K, $\xi_{\mathrm{TA}}^{(X)}$ is comparable to $\xi_{\mathrm{TO}}^{(X)}$; at low temperature, $\xi_{\mathrm{TA}}^{(X)}$ is less than half of $\xi_{\mathrm{TO}}^{(X)}$.

4. Comparison with experiment at high temperature

In Fig. 10, we compare our results for the absorption coefficient α with experimental results[42] at 77 and 300 K. Compared to the results near the band edge, the calculations without including excitonic effects fit the experiments better at high photon energy. The difference between theory and experiment at low photon energy can be attributed to excitonic effects and the temperature dependence of the indirect band gap energy, neglected in our calculation which takes that energy as its zero temperature value. Clearly, our neglect of excitonic effects and of this gap energy shift has less consequence at higher energies. In the calculation, we use the experimental frequency-dependent refractive index $n(\omega)$.[6] Because of the increase in phonon number, the absorption coefficient at 300 K is remarkably larger than at 77 K.
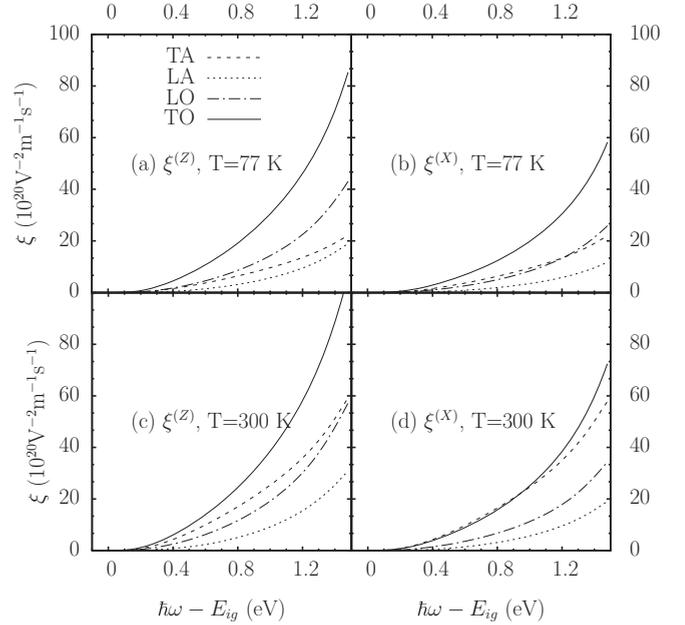

FIG. 9. Phonon-resolved $\xi^{(Z)}$ and $\xi^{(X)}$ at 77 K and 300 K.

5. Temperature dependence of carrier injection

Figure 11(a) gives the temperature dependence of the ratio $\xi(T)/\xi(0)$ (black solid curves), $\xi^{(X)}(T)/\xi^{(X)}(0)$ (green dash-dotted curves), and $\xi^{(Z)}(T)/\xi^{(Z)}(0)$ (red dashed curves) for $\hbar\omega - E_{\mathrm{ig}} = 70$, 100, and 1000 meV. The injection rates increase with temperature for all photon energies, and their slopes decrease with photon energy. When the temperature is lower than 70 K, the injection rates are almost independent of temperature, whereas they become nearly a linear function of temperature at temperature higher than 200 K. Their slopes depend on the photon energy with larger slopes at lower photon energies. The slopes for the injection in the Z and X valleys are found to differ at low photon energy, with the difference tending to disappear at high photon energy. The temperature dependence of phonon-resolved injection rates for excess photon energy 100 meV are plotted in Fig. 11(b). The temperature dependence of the phonon-resolved injection rates are similar to the total but show different slopes for different branches. In order to give a comprehensive understanding of
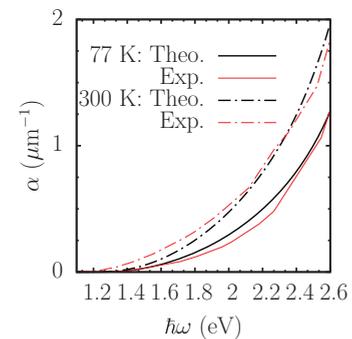

FIG. 10. (Color online) The comparison of α between our theory (thick curves) and experiments[42] (thin colored curves) at 77 K (solid curves) and 300 K (dash-dotted curves).

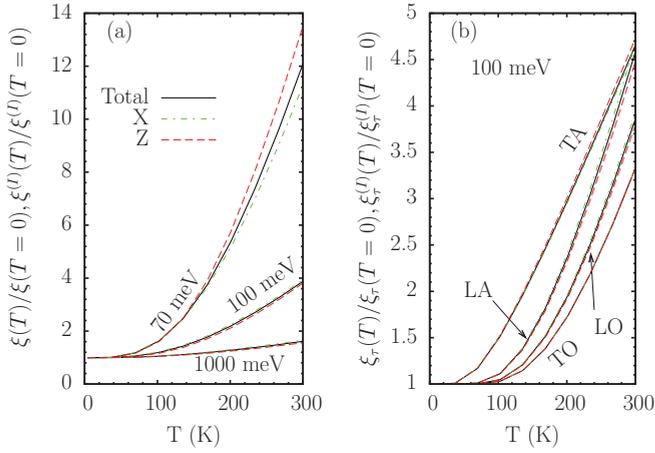FIG. 11. (Color online) (a) Temperature dependence of $\xi(T)/\xi(T=0)$, $\xi^{(X)}(T)/\xi^{(X)}(0)$, and $\xi^{(Z)}(T)/\xi^{(Z)}(0)$ for excess photon energy at 70, 100, and 1000 meV. (b) Temperature dependence of phonon resolved ratio for excess photon energy at 100 meV. (Black solid curves) The total injected carriers; (green dash-dotted curves) values in the X valley; (red dashed curves) values in the Z valley.

these results, we use the simplified formula for the band-edge injection in Eq. (11). At high temperature, the phonon number $N_{\bm{k}_c^0\lambda}$ is approximately $k_B T/\hbar\Omega_{\bm{k}_c^0\lambda}$, and Eq. (11) for absorption near the band edge can be rewritten as

$$\frac{\xi_{cv\lambda}^{(I)}(T,\omega)}{\xi_{cv\lambda}^{(I)}(0,\omega)} = 1 + \frac{k_B T}{\hbar\Omega_{\bm{k}_c^0\lambda}}\left[1 + \left(\frac{\hbar\omega - E_{\mathrm{ig}} + \hbar\Omega_{\bm{k}_c^0\lambda}}{\hbar\omega - E_{\mathrm{ig}} - \hbar\Omega_{\bm{k}_c^0\lambda}}\right)^2\right].$$

(26)

The linear dependence at high temperature is obvious. The slope is determined by the photon energy and decreases as the photon energy increases. At photon energy displayed in Fig. 11(b), however, the dependence of the slope on phonon energy is too complicated to be described by this simple formula.

B. Spin injection

1. Band-edge spin injection at 4 K

In Fig. 12(a) we show the spectra of the spin-injection rate in the Z valley (dashed curve) and the X valley (dash-dotted curve) as well as the total (solid curve) at 4 K. The spin-injection rates increase with photon energy and show strong valley anisotropy, as do in carrier injection. But the photon energy dependence of the spin-injection rates does not follow the quadratic JDOS but nearly a linear function. This indicates the strong wave-vector dependence of $\zeta_{c\bm{k}_cv\bm{k}_v\lambda}^{ab}$ given in Eq. (4). The injected spins in the X and Z valleys have opposite polarization direction. Fine structures of spin injection can be found from the DSP spectra given in Fig. 12(b). The total DSP at the band edge ($\hbar\omega_2 - E_{\mathrm{ig}} = 19$ meV, corresponding to the TA phonon emission process) is about -25%, while the DSP in the Z and X valleys approximates 0 and -32%. When the photon energy is higher than $\hbar\omega_2$, the spectra can be divided into three regions: (i) $\hbar\omega \in [\hbar\omega_2,\hbar\omega_3]$ with $\hbar\omega_3 - E_{\mathrm{ig}} = 57$ meV ($=\Omega_{\bm{k}_c^0,\mathrm{TO}}$). Here the DSP and the DSP$^{(X)}$ decrease rapidly with increasing energy to a minimum value of -1% and -5%, respectively, while the DSP$^{(Z)}$ increases to a maximum
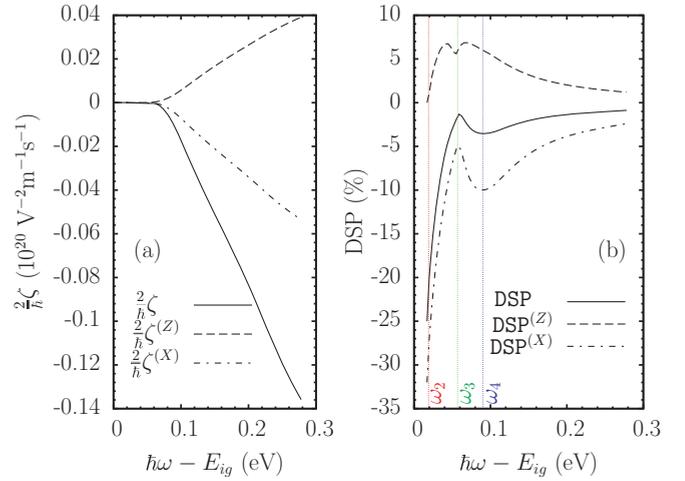

FIG. 12. (Color online) (a) Spectra of spin-injection rates ζ (solid curves), $\zeta^{(Z)}$ (dashed curves), and $\zeta^{(X)}$ (dash-dotted curves) at 4 K. (b) The corresponding DSP spectra. The labeled energies are $\hbar\omega_{2,3,4} - E_{\mathrm{ig}} = 19, 57, 90$ meV, respectively.

value of 5% when the photon energy is slightly smaller than $\hbar\omega_3$ and then decreases slightly to a local minimum at $\hbar\omega_3$. (ii) $\hbar\omega \in [\hbar\omega_3,\hbar\omega_4]$ with $\hbar\omega_4 - E_{\mathrm{ig}} = 90$ meV. Here the DSP and the DSP$^{(X)}$ increase to a maximum value -4% and -10%, and the DSP$^{(Z)}$ first slightly increases and then decreases. (iii) $\hbar\omega > \hbar\omega_4$. All DSP decrease monotonically to zero. The special photon energy $\hbar\omega_3$ is related to the TO phonon energy given in Sec. IV, and the features here are formed by the contributions from different phonon branches, which are plotted in Fig. 13.

According to the phonon energies, the injection edge energies of different phonon branches are ordered as TA < LA < LO < TO, which is obviously shown in Figs. 13(b)
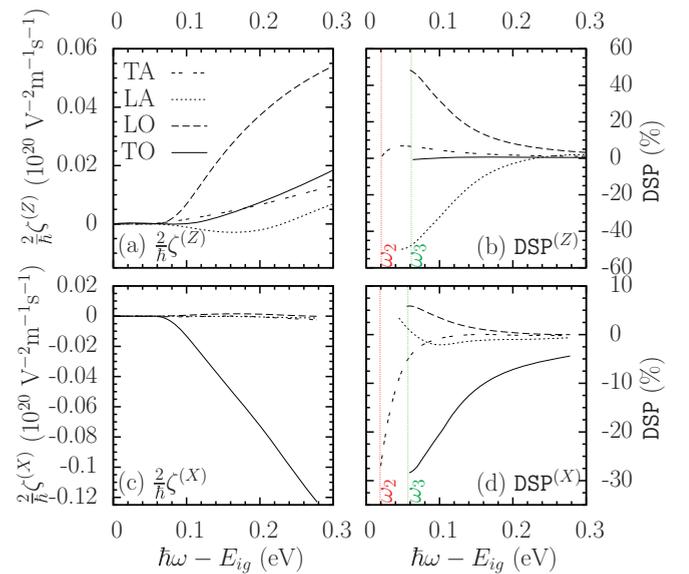

FIG. 13. (Color online) Phonon-resolved spin-injection rates [(a) and (c)] and DSP [(b) and (d)] in the Z [(a) and (b)] and X [(c) and (d)] valleys.

and 13(d). For the spin injection in the Z valley given in Fig. 13(a), the contributions from all phonon branches are almost of the same order of magnitude, even including the LA phonon branch, which gives a negligible contribution to carrier injection. Among these branches, the LO branch gives the largest contribution. The corresponding DSP are shown in Fig. 13(b). The DSP induced by TA branches starts from zero, reaches a maximum at about 45 meV above the onset of absorption, and then decreases, whereas the LA phonon branch contributes a negative spin-injection rate. LO and TO phonons take effect for $\hbar\omega > \hbar\omega_3$. Therefore, for the total DSP in the Z valley (in Fig. 12), the first increase to the maximum is induced by TA phonons, the following dip is induced by LA phonons, and the second peak is induced by LO phonons. Figures 13(c) and 13(d) give the spin-injection rates and DSP in the X valley. Here the contribution from the TO phonon branch dominates the spin injection, and those from other phonon branches give only minor contributions. As in the Z valley, the spin injection in the X valley (in Fig. 12) starts from the TA phonon branch; its DSP decreases with photon energy from a nonzero band-edge value and gives the fast decrease for photon energy in $\hbar\omega \in [\hbar\omega_2, \hbar\omega_3]$. At $\hbar\omega_3$ the TO phonons come into play, leading to injected electrons with a large spin polarization. As the contribution to the total spin polarization from these electrons begins to dominate, the DSP reaches a maximum at $\hbar\omega_4$ and decreases at high frequencies.

We now turn to resolving the spin-injection rates into contributions from different valence bands. The results are similar to the corresponding resolution of carrier injection rates. The HH band gives the largest contribution due to its large density of states, while the SO band gives the smallest. However, there are subtleties in the DSP of injected spins from each valence band. In Fig. 14 we give the valence band and phonon-resolved spectra of the DSP. While the band-edge values of the DSP are consistent with results in Table IV, the spin-polarization
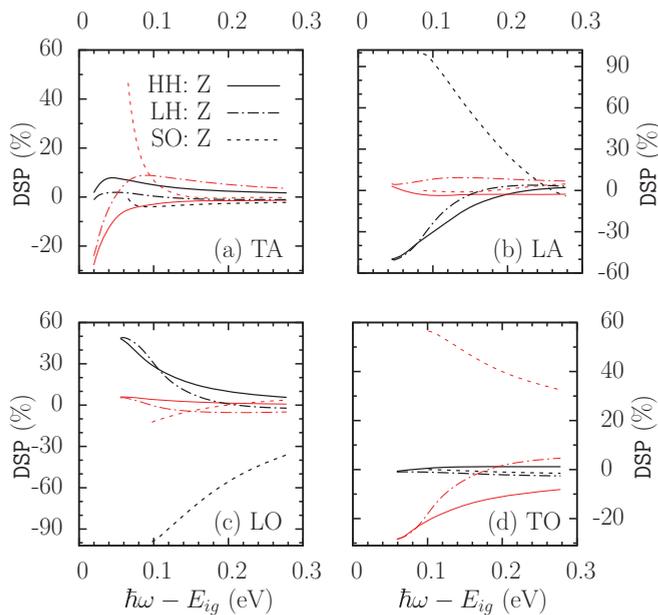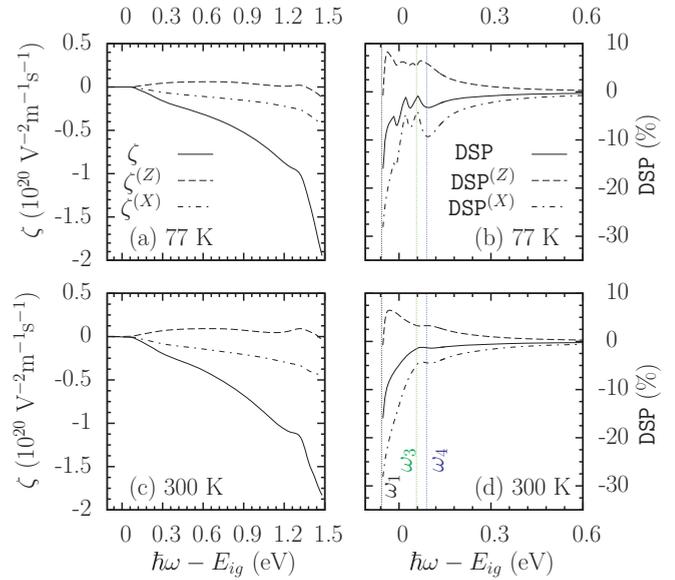

FIG. 15. (Color online) Spectra of spin-injection rates and DSP at 77 K and 300 K; $\hbar\omega_1 - E_{ig} = -57$ meV.

direction shows a complicated energy dependence based on whether the band edge DSP is zero. For processes with nonzero band-edge values, the DSP decrease from the nonzero values. For processes with zero band-edge values, the DSP increase to a maximum value and then decrease. Some of these DSP change sign with increasing photon energy.

2. Spin injection at high temperature

In Fig. 15 we plot the spectra of spin-injection rates at 77 K and 300 K. In contrast to the carrier injection rates, which increase considerably from 77 K to 300 K, both the total spin-injection rates and the rates in each valley change little from 77 K [Fig. 15(a)] to 300 K [Fig. 15(c)]. In order to show clearly the spin injection at the injection edge, the DSP are plotted in Figs. 15(b) and 15(d), respectively. The phonon absorption process becomes increasingly important as the temperature rises and is shown by the left shifts of the onset of DSP to $\hbar\omega_1$, which is determined by the TO/LO phonon absorption processes. In addition, the peak appearing at $\hbar\omega_4$ and 4 K in Fig. 12(b) becomes fairly obscure at high temperature. These results can be better understood from the phonon-resolved DSP spectra at 300 K, given in Fig. 16.

For the spin-injection rates in the Z valley, shown in Fig. 16(a), the contribution from each phonon branch is still of the same order of magnitude, but the TO phonon-assisted process dominates the injection at high photon energy. For the spin-injection rates in the X valley, shown in Fig. 16(c), the contribution from the TO phonon branch dominates for all photon energies. However, the DSP, plotted in Figs. 16(b) and 16(d), show finer structure in the low photon energy region than the DSP at 4 K. The fine structure is induced by the combined effect of the phonon emission and phonon absorption processes, which take effect at 300 K with considerable equilibrium phonon numbers for all phonon branches. According to the simplified Eq. (11), the injection rates for phonon absorption/emission processes differ from the JDOS,
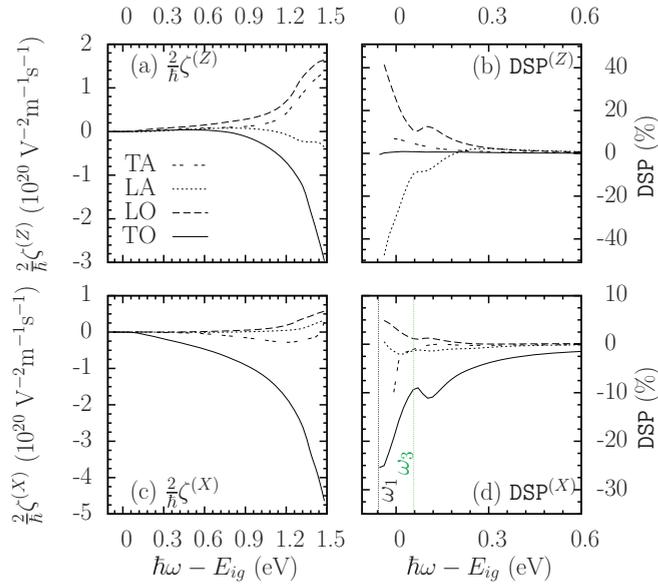

FIG. 14. (Color online) Phonon and valence band resolved DSP in the Z valley (thick curves) and X valley (thin colored curves).

FIG. 16. (Color online) Phonon-resolved spectra of spin-injection rates and DSP at 300 K.

$J_{cv\lambda}(\hbar\omega \mp \hbar\Omega_{\boldsymbol{k}_c^0\lambda})$, at low photon energy. Therefore, spectra of DSP for these two processes have similar line shapes, except for a phonon energy shift left or right. This conclusion is confirmed by our numerical results, shown in Fig. 17. Here the DSP from TO phonon absorption and emission processes are plotted for spins in both Z and X valleys at 300 K, and all the absorption curves are right shifted by $2\Omega_{\boldsymbol{k}_c^0,\mathrm{TO}}$. The overlap is obvious. Based on these results, we return to Fig. 16.

We consider the DSP from the TO phonon-assisted process in the X valley, shown as a solid curve in Fig. 16(d). The spectrum in $[\hbar\omega_1,\hbar\omega_3]$ is induced by the phonon absorption processes and decreases with increasing photon energy. When the photon energy is higher than $\hbar\omega_3$, the TO phonon emission process comes into play. However, the spin-injection rate for phonon emission is approximately proportional to $1 + N_{\boldsymbol{k}_c^0,\mathrm{TO}}$, while that for phonon absorption is proportional to $N_{\boldsymbol{k}_c^0,\mathrm{TO}}$; thus the former gives much larger injection rates than the latter. This results in a peak in the total DSP for the TO phonon-assisted process at energies where phonon emission becomes important.
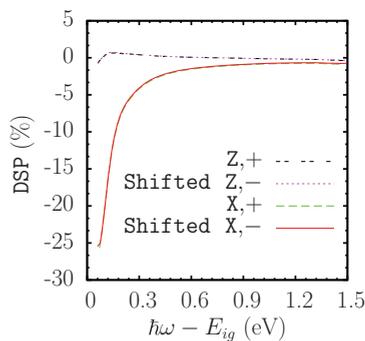

FIG. 17. (Color online) Spectra of DSP for TO phonon absorption and emission processes in the Z and X valleys at 300 K.
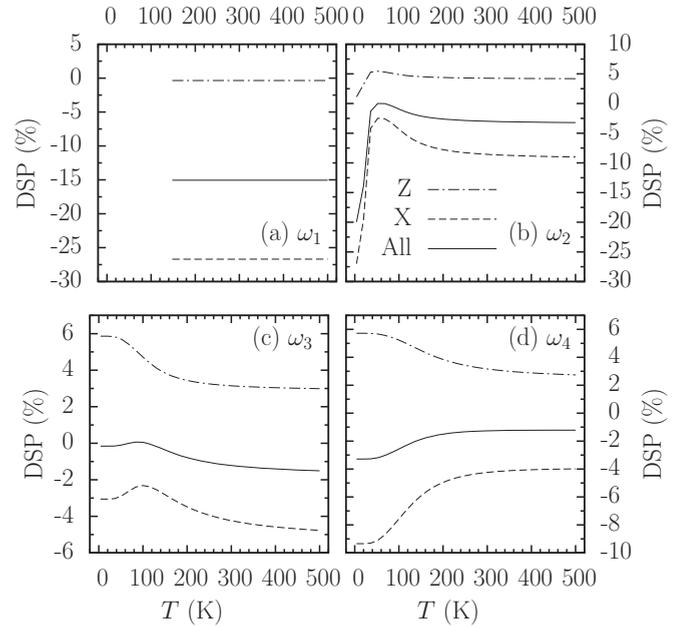

FIG. 18. Temperature dependence of $\mathrm{DSP}^{(Z)}$ (dot-dashed curves), $\mathrm{DSP}^{(X)}$ (dashed curves), as well as the total DSP (solid curves) at photon energies $\hbar\omega_{1-4}$.

3. Temperature dependence of spin injection

Figure 18 shows the temperature dependence of the DSP at the different photon energies $\hbar\omega_{1-4}$. For photon energy $\hbar\omega_1$, all DSPs are temperature independent: The TO phonon absorption process is the only process at this photon energy, and the injection rates of carriers and spins are approximately proportional to $N_{\boldsymbol{k}_c^0,\mathrm{TO}}$; the two rates therefore scale the same with temperature, leading to a temperature-independent DSP. We check the temperature dependence of the DSP for all phonon branches at photon energy $\hbar\omega - E_{\mathrm{ig}} = 100$ eV in Fig. 19. All these DSP are independent of temperature. This conclusion is valid for all photon energies considered to this point in this paper. However, the total DSP, shown in Figs. 18(b)–18(d), *are* temperature dependent. At the indicated photon energies, more than one phonon branch makes a contribution. The injection rates for different phonon branches have different temperature dependences due to the different phonon energies. The ratio between the total injection rates of carriers and spins, i.e., the DSP, thus becomes temperature
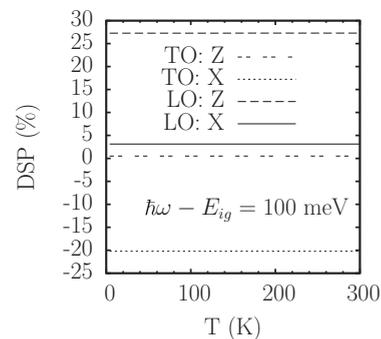

FIG. 19. Temperature dependence of the DSP for TO and LO phonon-emission-assisted processes.

dependent. At high temperature, $N_{q\lambda} \propto T$ is approximately valid for all phonon branches, so the injection coefficients of ξ and ζ are approximately proportional to T and give a constant DSP as saturation value. This is shown in Fig. 18.

VII. CONCLUSION

In conclusion, we have performed a full band structure calculation to investigate the indirect optical carrier and spin injection in bulk silicon. The injection spectra for carriers, spins, and DSP in each valley are studied in detail at different temperatures. The indirect gap injection is dominated by the transition from the HH band to the lowest conduction band due to the large JDOS. When incident light is propagating along one principal axis, the injection shows strong valley anisotropy. The injection rates induced by each phonon-assisted process increase with temperature. For carrier injection, we find that in the Z valley the TO phonon-assisted process dominates up to 300 K; in the X valley, it only dominates at low temperature, whereas the injection rates induced by the TA phonon-assisted process increases to a comparable value at 300 K. The higher the photon energy, the weaker the temperature dependence. For spin injection, we find that injected spins in the Z and X valleys have opposite polarization directions. In the Z valley, the LO phonon-assisted process dominates around the band edge, while the TO phonon-assisted process dominates at high photon energy; in the X valley, the TO phonon-assisted process dominates for all photon energies.

The calculated absorption coefficients are in good agreement with experiments at high photon energy. Experience from direct gap absorption might lead one to believe this would not hold, since first-principle studies of direct optical absorption in Si and GaAs[43–45] demonstrated that the electron-hole interaction plays an important role even for high photon energy. Full band structure calculations of indirect gap absorption, including electron-hole interactions, have yet to be done, and the effect of these interaction on the indirect absorption coefficient at high photon energies have yet to be established. In any event, since to first approximation the nearly spin-independent electron-hole interaction will modify spin and carrier injections in the same way, it is reasonable to expect that the DSP of injected electrons in exciton continuum states will be insensitive to this interaction, which we neglect. Future work to confirm this is clearly in order, but in the interim we feel our study constitutes a good first investigation.

The DSP spectra excibit a rich variety of behaviors. At 4 K, the maximum DSP is about -25% for photon energy $E_{\text{ig}} + \Omega_{\boldsymbol{k}_c^0,\text{TA}}$; absorption at this temperature and energy is dominant by a TA phonon emission process. With increasing temperature, the phonon absorption processes become important, and the DSP for this photon energy decreases quickly. At 300 K, the maximum DSP appears at the photon energy $E_{\text{ig}} - \Omega_{\boldsymbol{k}_c^0,\text{TO}}$ as a value -15%, which only comes from the TO phonon absorption assisted process and is temperature-independent. The DSP in the X valley can reach a maximum value -32% at 4 K and -26% at 300 K; both are larger than the total value and the value in the Z valley. Compared to bulk silicon, it should therefore be more efficient to inject spin in a confined silicon structure, where conduction band valleys are split.

APPENDIX: MODIFIED TETRAHEDRON SUMMATION

Both Eq. (6) and the JDOS in Eq. (12) are of the following form

$$X(\omega) = \int_{V_c'} d\boldsymbol{k}_c \int_{V_v'} d\boldsymbol{k}_v \delta(\varepsilon_{\boldsymbol{k}_c} - \varepsilon_{\boldsymbol{k}_v} + \hbar\Omega_{\boldsymbol{k}_c - \boldsymbol{k}_v} - \hbar\omega)$$
$$\times X(\boldsymbol{k}_c, \boldsymbol{k}_v). \tag{A1}$$

Here the integration spaces V_c' and V_v' are the irreducible BZ wedges, which are confined by the Γ, X, L, $U(K)$, and W points of a fcc Brillouin zone. Our numerical scheme is based on the improved LATM.[24,35] We divide V_c' (V_v') into N_c (N_v) small tetrahedra as $V_c' = \sum_{i=1}^{N_c} V_{c,i}'$ ($V_v' = \sum_{j=1}^{N_v} V_{c,j}'$) with vertices $\boldsymbol{k}_{c,I}, I = 1, \ldots, M_c$ ($\boldsymbol{k}_{v,J}, J = 1, \ldots, M_v$). By a simple transformation, Eq. (A1) becomes

$$X(\omega) = \sum_{ij} \int d\epsilon \, X_{ij}(\omega, \epsilon),$$

with

$$X_{ij}(\omega, \epsilon) = \int_{V_{c,i}'} d\boldsymbol{k}_c \delta(\varepsilon_{\boldsymbol{k}_c} - \epsilon) Y_j(\boldsymbol{k}_c, \hbar\omega - \hbar\bar{\Omega}_{ij} - \epsilon) \tag{A2}$$

and

$$Y_j(\boldsymbol{k}_c, \epsilon) = \int_{V_{v,j}'} d\boldsymbol{k}_v \delta(\varepsilon_{\boldsymbol{k}_v} - \epsilon) X(\boldsymbol{k}_c, \boldsymbol{k}_v). \tag{A3}$$

In obtaining the equations above, we approximate the phonon energy to be a fixed value $\hbar\bar{\Omega}_{ij}$ between the two small tetrahedra $V_{c,i}'$ and $V_{v,j}'$. Now the Eqs. (A2) and (A3) have the same shape, so we only discuss Eq. (A3) in the following. Though the tetrahedron method can be applied to Eq. (A3) directly, we avoid doing this because the transition matrix elements are obtained within the scheme of the EPM, which are very time-consuming in calculation for each $(\boldsymbol{k}_{c,I}, \boldsymbol{k}_{v,J})$ pair. However, the direct tetrahedron method needs more $\boldsymbol{k}$ points for convergence than is computationally feasible. Instead, since the dependence of the transition matrix elements on $\boldsymbol{k}_c$ and $\boldsymbol{k}_v$ is weak, we linearly interpolate $X(\boldsymbol{k}_c, \boldsymbol{k}_v)$ in tetrahedron $V_{v,j}'$ as

$$X(\boldsymbol{k}_c, \boldsymbol{k}_v) = \sum_{m=1}^{4} X(\boldsymbol{k}_c, \boldsymbol{k}_{v,j}^m) F_{v,j}^m(\boldsymbol{k}_v),$$

with $\boldsymbol{k}_{v,j}^m$ being the position of four vertices of this tetrahedron and $F_{v,j}^m(\boldsymbol{k}_v)$ being the linear interpolation function related to

the mth vertex. Then Eq. (A3) becomes

$$Y_j(\boldsymbol{k}_c, \epsilon) = \sum_{m=1}^{4} w_{v,j}^m(\epsilon) X(\boldsymbol{k}_c, \boldsymbol{k}_{v,j}^m),$$

$$w_{v,j}^m(\epsilon) = \int_{V_{v,j}'} d\boldsymbol{k}_v \delta(\varepsilon_{v\boldsymbol{k}_v} - \epsilon) F_{v,j}^m(\boldsymbol{k}_v). \quad \text{(A4)}$$

In the same way, we get $w_{c,i}^n(\epsilon)$ for Eq. (A2). Then we find

$$X_{ij}(\omega, \epsilon) = \sum_{nm=1}^{4} w_{c,i}^n(\epsilon) w_{v,j}^m(\hbar\omega - \hbar\Omega_{\boldsymbol{k}_{c,i}^n - \boldsymbol{k}_{v,j}^m} - \epsilon)$$
$$\times X(\boldsymbol{k}_{c,i}^n, \boldsymbol{k}_{v,j}^m)$$

and

$$X(\omega) = \int d\epsilon \sum_{IJ} W_{c,I}(\epsilon) W_{v,J}(\hbar\omega - \hbar\Omega_{\boldsymbol{k}_{c,I} - \boldsymbol{k}_{v,J}} - \epsilon)$$
$$\times X(\boldsymbol{k}_{c,I}, \boldsymbol{k}_{v,J}), \quad \text{(A5)}$$

with

$$W_{c,I}(\epsilon) = \sum_{in, \boldsymbol{k}_{c,i}^n = \boldsymbol{k}_{c,I}} w_{c,i}^n(\epsilon),$$

$$W_{v,J}(\epsilon) = \sum_{jm, \boldsymbol{k}_{v,j}^n = \boldsymbol{k}_{v,J}} w_{v,j}^n(\epsilon). \quad \text{(A6)}$$

In the above equations, we replace $\hbar\Omega_{\boldsymbol{k}_{c,i}^n - \boldsymbol{k}_{v,j}^m}$ by $\hbar\bar{\Omega}_{ij}$.

In indirect absorption, the excited holes are located around the top of the valence band, while the electrons are around the band edge of the conduction band. So we use a different division for $\boldsymbol{k}_c$ and $\boldsymbol{k}_v$. With the division points $\boldsymbol{k}_{c,I}$ and $\boldsymbol{k}_{v,J}$, we use the Delaunay triangulation method from the CGAL package[46] to set up the tetrahedra. In these tetrahedra, the weights $w_{v,j}^m$ and $w_{c,i}^n$ can be calculated. However, the integration includes a δ function, which is a fast-varying function in $\boldsymbol{k}$ space, and the present tetrahedron is too rough to obtain the weights with required precision. We refine this tetrahedron into smaller ones.

In our calculation, the division depends on the band structure. For conduction bands and the heavy hole band, $\boldsymbol{k}_{c,I}$ or $\boldsymbol{k}_{v,J}$ are generated with their distance not larger than $0.05 \times \frac{2\pi}{a}$, while for light hole and spin split-off bands, the distances become $0.04 \times \frac{2\pi}{a}$ and $0.02 \times \frac{2\pi}{a}$, respectively. For the heavy hole grid, the accurate weights can be obtained by refining each tetrahedron as 8^3 smaller ones (each edge is refined into eight parts).

The convergence of the results is examined for the injection from heavy hole band to conduction band by changing the division points distance to $0.025 \times \frac{2\pi}{a}$. The difference between the injection rates from these two divisions is less than 5%.

---

*Author to whom correspondence should be addressed: sipe@physics.utoronto.ca

[1] F. Meier and B. Zakharchenya, *Optical Orientation* (North-Holland, Amsterdam, 1984).

[2] I. Žutić, J. Fabian, and S. Das Sarma, Rev. Mod. Phys. **76**, 323 (2004).

[3] J. Fabian, A. M. Abiague, C. Ertler, P. Stano, and I. Žutić, Acta Phys. Slovaca **57**, 565 (2007).

[4] M. W. Wu, J. H. Jiang, and M. Q. Weng, Phys. Rep. **493**, 61 (2010).

[5] G. G. Macfarlane, T. P. McLean, J. E. Quarrington, and V. Roberts, Phys. Rev. **111**, 1245 (1958).

[6] M. A. Green and M. J. Keevers, Prog. Photovolt: Res. Appl. **3**, 189 (1995).

[7] T. Suemoto, K. Tanaka, A. Nakajima, and T. Itakura, Phys. Rev. Lett. **70**, 3659 (1993).

[8] V. Y. Mendeleyev, S. N. Skovorodko, E. N. Lubnin, and V. M. Prosvirikov, Appl. Phys. Lett. **93**, 131916 (2008).

[9] M. Sarıtaş and H. D. McKell, J. Appl. Phys. **61**, 4923 (1987).

[10] H. A. Weakliem and D. Redfield, J. Appl. Phys. **50**, 1491 (1979).

[11] R. J. Elliott, Phys. Rev. **108**, 1384 (1957).

[12] B. Y. Lao, J. D. Dow, and F. C. Weinstein, Phys. Rev. B **4**, 4424 (1971).

[13] B. Y. Lao, J. D. Dow, and F. C. Weinstein, Phys. Rev. Lett. **26**, 499 (1971).

[14] V. D. Kulakovskiĭ, G. E. Pikus, and V. B. Timofeev, Sov. Phys. Usp. **24**, 815 (1981).

[15] R. L. Hartman, Phys. Rev. **127**, 765 (1962).

[16] D. Dunn, Phys. Rev. **166**, 822 (1968).

[17] W. S. Chow, Phys. Rev. **185**, 1056 (1969).

[18] W. S. Chow, Phys. Rev. **185**, 1062 (1969).

[19] O. J. Glembocki and F. H. Pollak, Phys. Rev. Lett. **48**, 413 (1982).

[20] S. Bednarek and U. Rössler, Phys. Rev. Lett. **48**, 1296 (1982).

[21] M.-F. Li, Z.-Q. Gu, and J.-Q. Wang, Phys. Rev. B **42**, 5714 (1990).

[22] O. J. Glembocki and F. H. Pollak, Phys. Rev. B **25**, 1193 (1982).

[23] M. Klenner, C. Falter, and W. Ludwig, Ann. Phys. **504**, 24 (1992).

[24] F. Nastos, J. Rioux, M. Strimas-Mackey, B. S. Mendoza, and J. E. Sipe, Phys. Rev. B **76**, 205113 (2007).

[25] G. Lampel, Phys. Rev. Lett. **20**, 491 (1968).

[26] G. Lampel, Proc. 9th Int. Conf. Phys. Semicond. **2**, 1139 (1968).

[27] A. S. Verhulst, Ph.D. thesis, Stanford University, 2004.

[28] P. Li and H. Dery, Phys. Rev. Lett. **105**, 037204 (2010).

[29] J. R. Chelikowsky and M. L. Cohen, Phys. Rev. B **10**, 5095 (1974).

[30] J. R. Chelikowsky and M. L. Cohen, Phys. Rev. B **14**, 556 (1976).

[31] G. Weisz, Phys. Rev. **149**, 504 (1966).

[32] W. Weber, Phys. Rev. B **15**, 4789 (1977).

[33] J. Rioux and J. E. Sipe, Phys. Rev. B **81**, 155215 (2010).

[34] J. L. Cheng, M. W. Wu, and J. Fabian, Phys. Rev. Lett. **104**, 016601 (2010).

[35] P. E. Blöchl, O. Jepsen, and O. K. Andersen, Phys. Rev. B **49**, 16223 (1994).

[36] P. Y. Yu and M. Cardona, *Fundamentals of Semiconductors: Physics and Materials Properties* (Springer, Berlin, 2005).

[37] P. Lautenschlager, P. B. Allen, and M. Cardona, Phys. Rev. B **31**, 2163 (1985).

[38] G. D. Mahan, J. Appl. Phys. **51**, 2634 (1980).

[39] W. Bludau, A. Onton, and W. Heinke, J. Appl. Phys. **45**, 1846 (1974).

[40]V. Alex, S. Finkbeiner, and J. Weber, J. Appl. Phys. **79**, 6943 (1996).

[41]M. M. Rieger and P. Vogl, Phys. Rev. B **48**, 14276 (1993).

[42]S. M. Sze, *Physics of Semiconductor Devices* (John Wiley & Sons, New York, 1981).

[43]M. Rohlfing and S. G. Louie, Phys. Rev. B **62**, 4927 (2000).

[44]G. Onida, L. Reining, and A. Rubio, Rev. Mod. Phys. **74**, 601 (2002).

[45]R. Leitsmann, W. G. Schmidt, P. H. Hahn, and F. Bechstedt, Phys. Rev. B **71**, 195209 (2005).

[46]CGAL, Computational Geometry Algorithms Library [http://www.cgal.org].